JOURNAL OF THERMOPHYSICS AND HEAT TRANSFER
Vol. 14, No. 1, January–March 2000

Numerical Thermal Model of Resistance Spot Welding in Aluminum

Jamil A. Khan* and Kirk Broach†
University of South Carolina, Columbia, South Carolina 29208
and
A. A. S. Arefin Kabir‡
ESAB Welding and Cutting Products, Florence, South Carolina 2501-0545

A three-dimensional thermal model for resistance spot welding in aluminum is presented. The numerical model, validated with experimental findings, considered phase change and the associated weld pool convection. A parametric study was performed to determine the influence of welding features such as welding current, faying surface (workpiece contact surface) electrical contact resistance, and electrode–workpiece (E/W) thermal contact conductance. These parameters have significant effects on the nugget and heat-affected-zone geometry. The phase change morphology, including melting and solidification rates and weld pool dynamics, was also significantly influenced by the parameters studied. The strongest convection was observed at the center of the molten pool in a vertical plane, aligned with gravity. Although two prominent convection cells developed, the phase change morphology was not significantly affected by convection due to the short welding time (less than 0.1 s) and low fluid velocity (smaller than 0.01 mm/s). The nugget grew nonlinearly with increasing current and faying surface electrical contact resistance, whereas it diminished with increasing E/W thermal contact conductance. The influence of electrical contact resistance at the faying surface on nugget size was less pronounced than that of the other parameters. The length of time that the weld pool existed was directly proportional to current and indirectly proportional to E/W thermal contact conductance.

Nomenclature

A = porosity function for the momentum equations
C = morphology constant
C_p = specific heat, J/kg-K
g = acceleration due to gravity, m/s^2
h = convective heat transfer coefficient, W/m^2-K
h_s = sensible enthalpy, J/kg
$\hat{h}$ = total enthalpy, J/kg
I = welding current, ac, A
I_m = maximum peak value of ac current, A
k = thermal conductivity, W/m-K
L = latent heat of fusion, J/kg
$\hat{n}$ = direction normal to a surface
Q = volumetric source term for heat generating control volumes, W/m^3
R_∞ = static contact resistance, Ω
r = radial distance from electrode axis, m
r_e = electrode radius, m
T = temperature, K
t = time, s
U_e = electrode to workpiece conductance, W/m^2-K
u, v, w = velocity components in x, y, and z directions, m/s
X_L = length of calculation domain, m
x, y, z = coordinates
Y_L = height of calculation domain, m
Z_L = width of calculation domain, m
α = thermal diffusivity, $k/\rho C_p$, m^2/s
β = volumetric coefficient of thermal expansion, 1/K
γ = liquid fraction
ΔH = nodal latent heat, J/kg
δ = gap between workpiece surface and coolant, m
ε = porosity of computational cell, $\Delta H/L$
ε_f = separation gap at faying surface, m
λ = relaxation factor
μ = dynamic viscosity, N-s/m^2
ρ = density for momentum equation and capacitance for energy equation, kg/m^3
σ = electrical conductivity, mho

Subscripts

cl = coolant
e = electrode
m = melting point
wp = workpiece
wps = workpiece surface
∞ = ambient

Introduction

RESISTANCE spot welding (RSW) is a widely used joining process that involves complex heat and mass transfers combined with electrical, mechanical, and metallurgical phenomena. The metal sheets to be joined are brought together under pressure by a pair of water-cooled electrodes. A high electric current is passed through the metal sheets between the electrodes for a short duration. The flow of current through the contact resistance at the faying surface and joule heating in the metal sheets produce a molten weld pool at the interface. Conduction through the electrodes and free surface convection to the ambient air cool the workpieces. The metal sheets are then joined as the weld pool solidifies. Although RSW has been extensively studied, nearly all efforts have focused on steel sheets. Aluminum typically has higher thermal and electrical conductivities and varied metallurgical properties and oxide layers that influence electrical contact at the faying surface. These differing properties result in drastically different melting and solidification rates, nugget shapes, heat-affected zones, and weld pool dynamics.

Heat transfer with phase change is an important aspect of research into RSW, which involves melting and solidification of the metal workpieces. Viskanta,[1–3] Yao and Prusa,[4] and Fukusako and

---

Received 30 April 1999; revision received 9 August 1999; accepted for publication 16 August 1999. Copyright © 1999 by the American Institute of Aeronautics and Astronautics, Inc. All rights reserved.

*Associate Professor, Laboratory for Applied Heat Transfer, Department of Mechanical Engineering; jamil.khan@sc.edu.

†Graduate Student, Laboratory for Applied Heat Transfer, Department of Mechanical Engineering.

‡Mechanical Engineering, P.O. Box 100545, 411 South Ebenezer Road.

Yamada[5] provide extensive literature on different aspects of solidification and melting heat transfer. Brent et al.[6] numerically predicted the melting and solidification of pure metal. Computational cells undergoing a change of phase were modeled as pseudoporous media with porosity, ranging between one and zero, as a function of the change of nodal latent heat. Gau and Viskanta[7] experimentally studied the melting of gallium in a two-dimensional cavity. Brent et al.[6] predicted similar results from their numerical model for the melting of gallium.

Nugget growth during the RSW process can be predicted using an efficient melting and solidification model. Gould[8] studied nugget growth during RSW in steel with a one-dimensional, finite difference model and compared his predictions with experimental results. The difference between the predicted and the measured nugget thicknesses and the nugget growth was suggested to be due to the model's inability to account for radial heat flow into the workpieces and underestimation of the heat generation at the faying surface. Neid[9] and Tsai et al.[10] modeled resistance spot welding in stainless steel using the finite element technique. Both studies were primarily applied toward understanding the thermal–mechanical interaction during electrode squeezing. Tsai et al.[10] studied the effect of unequal workpiece thickness, as well as the effect of dissimilar materials on nugget growth and shape. Both of the models[9,10] were axisymmetric conduction models.

Browne et al.[11] developed an axisymmetric model for resistance spot welding in aluminum alloys. Their simulation included joule heating and thermal conduction, as well as elastic–plastic mechanical deformation. It was shown that the value of the contact resistance and the faying surface contact area that caused the interfacial heating had a large effect on nugget formation in the RSW of aluminum. Wei and Ho,[12] Wei and Yeh,[13] and Wei et al.[14] published a series of papers on thermal modeling of spot welding in steel. A conduction model was used to compare the calculated weld nugget growth, thickness, and shape with experimental data.[12] Fluid patterns, temperature fields, and solute distributions in the liquid, solid, and mushy zones were investigated for RSW.[13] Property variations were shown to strongly affect the nugget growth, and the maximum weld pool velocity reported was about 5 mm/s. The authors[14] presented the effect of electrode radius and cone angle, parameters governing electric current, electrical conductivity ratio, and electrical contact resistance on transport phenomena during resistance spot welding. They used the finite difference technique and the assumption of axisymmetry in the aforementioned models.

RSW is used in a variety of systems including automobile, spacecraft, shell, and tank manufacturing. Experiments of RSW are tedious due to the high current involved (greater than 20 kA for aluminum) and the fast processing time (6–12 cycles). The RSW of aluminum is more complicated than that of steel due to factors including electrical and thermal conductivities, Young's modulus, dynamic contact resistance, plastic temperature range, and thermal expansion.[15,16] The higher electrical and thermal conductivities encountered in aluminum alloys require three to four times the welding current than that for steel sheets with similar thickness. Aluminum is more susceptible to surface indention from electrode contact due to its low Young's modulus, approximately one-third that of steel. The dynamic contact resistance, which changes with temperature and the formation of various oxide layers, significantly affects the weldability of aluminum. Expulsion of the molten metal from the weld pool is more likely due to a narrower plastic temperature range, approximately 93°C, compared with 583°C for steel. As a result, acceptable nuggets are more difficult to obtain and require precise welding schedules. Finally, aluminum requires greater electrode forces to contain the molten pool and to ensure workpiece contact due to the higher thermal expansion. A significant force is also necessary to forge the molten pool during solidification to prevent cracking of the weld. Thus, a quantitatively consistent thermal model is needed to provide insight into this joining process. Such a model could be further extended to predict nugget formation in aluminum alloys.

In the present study, a three-dimensional numerical model for RSW is developed by applying the enthalpy porosity technique described by Brent et al.[6] To validate the numerical model, experiments were performed on 1000-series aluminum sheets. A parametric study of various welding features including current, faying surface electrical contact resistance, and E/W thermal contact conductance was performed with the validated model to provide a better understanding of RSW in aluminum.

System Model and Analysis

Figure 1 shows a schematic diagram of the RSW considered for the present study. The workpieces are pure aluminum of equal thickness. The copper electrodes are of length 1 with flat faces of radius r_e. Each electrode has a coolant jacket 3 mm away from the E/W interface. Heat transfer through the electrode is calculated numerically with a two-dimensional, implicit finite difference model using a constant thermal E/W contact resistance. A high welding current passes through the workpieces between the electrodes, and the resulting generated energy initiates a weld nugget at the faying surface. The nugget forms primarily due to the heat generated by the contact resistance between the workpieces and secondarily due to joule heating of the sheets. A schematic diagram of the regions that experience joule and interfacial heating is shown in Fig. 2. The boundary conditions for the calculation domain are also presented. Phase change is modeled with a single-domain, enthalpy-porosity technique. Calculation of the phase change interface is implicit and does not require an explicit phase-front tracking. Instead, the solid–liquid interface is treated as a mushy zone with the width of one control volume (isothermal melting). The details of this procedure are provided in Ref. 6.

The fluid flow is assumed laminar due to the small velocities encountered in the present study and as reported in the literature.[13] The Reynolds number, based on the maximum obtained velocity and the workpiece thickness as the length scale, is less than 10. As in Ref. 6, the Boussinesq approximation for natural convection is considered

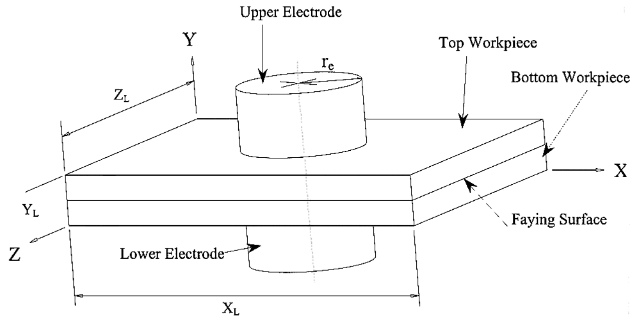

Fig. 1 Schematic diagram of resistance spot welding and coordinate system.

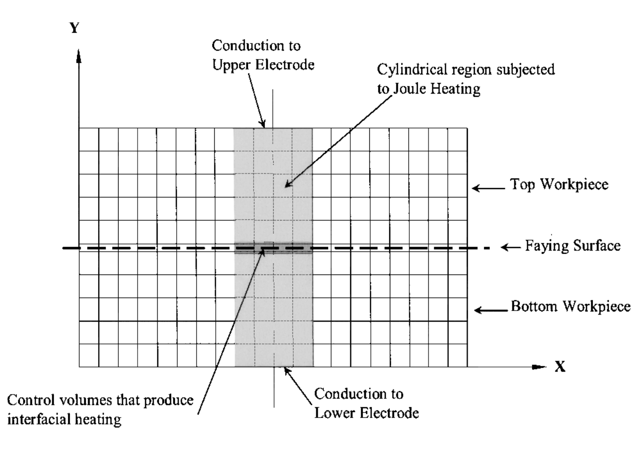

All exposed outer surface experience convection to the ambient.

Fig. 2 Central vertical cross section for calculation domain and boundary conditions (schematic).

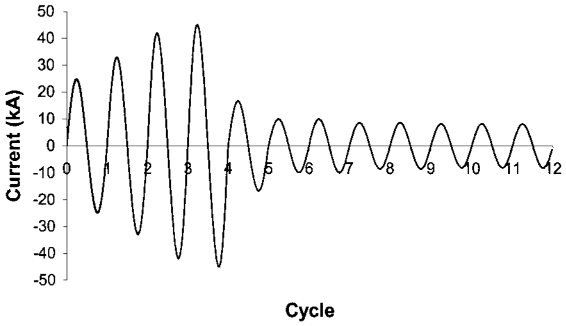

Fig. 3 Weld schedule used for resistance spot welding; maximum amplitude I_m 45 kA.

to be valid. A suitable weld schedule was adapted for the experiments of 1000-series aluminum utilizing the current shown in Fig. 3. The same weld schedule is used for the parametric study. Current density is assumed to be uniform across the area of contact acting along the electrode axis. Electrical conductivity of the workpiece is considered to be a function of the temperature, reducing asymptotically to the melting temperature where it is defined as constant in the liquid region. The effect of electrode pressure and surface condition on the electrical contact resistance is not considered at the present time. Heating due to contact resistance at the E/W interface is ignored because experimental measurement has shown that it is low compared to the faying surface contact resistance.[17] The effect of surface tension is not taken into account because the molten pool formed during phase change does not have any free surfaces.

Governing Equations

With the preceding assumptions, the time-dependent conservation equations for mass, momentum, and energy can be written as follows.

Continuity:

$$\frac{\partial}{\partial x}(\rho u) + \frac{\partial}{\partial y}(\rho v) + \frac{\partial}{\partial z}(\rho w) = 0 \tag{1}$$

X momentum:

$$\frac{\partial}{\partial t}(\rho u) + \frac{\partial}{\partial x}(\rho uu) + \frac{\partial}{\partial y}(\rho vu) + \frac{\partial}{\partial z}(\rho wu) = \frac{\partial}{\partial x}\left(\mu\frac{\partial u}{\partial x}\right) + \frac{\partial}{\partial y}\left(\mu\frac{\partial u}{\partial y}\right) + \frac{\partial}{\partial z}\left(\mu\frac{\partial u}{\partial z}\right) - \frac{\partial P}{\partial x} + Au \tag{2}$$

Y momentum:

$$\frac{\partial}{\partial t}(\rho v) + \frac{\partial}{\partial x}(\rho uv) + \frac{\partial}{\partial y}(\rho vv) + \frac{\partial}{\partial z}(\rho wv) = \frac{\partial}{\partial x}\left(\mu\frac{\partial v}{\partial x}\right) + \frac{\partial}{\partial y}\left(\mu\frac{\partial v}{\partial y}\right) + \frac{\partial}{\partial z}\left(\mu\frac{\partial v}{\partial z}\right) - \frac{\partial P}{\partial y} + Av + \rho g\beta(T - T_m) \tag{3}$$

Z momentum:

$$\frac{\partial}{\partial t}(\rho w) + \frac{\partial}{\partial x}(\rho uw) + \frac{\partial}{\partial y}(\rho vw) + \frac{\partial}{\partial z}(\rho ww) = \frac{\partial}{\partial x}\left(\mu\frac{\partial w}{\partial x}\right) + \frac{\partial}{\partial y}\left(\mu\frac{\partial w}{\partial y}\right) + \frac{\partial}{\partial z}\left(\mu\frac{\partial w}{\partial z}\right) - \frac{\partial P}{\partial w} + Aw \tag{4}$$

where A is given by

$$A = \frac{-C(1-\varepsilon)}{\varepsilon^3 + b} \tag{5}$$

where C is a constant for a given material and a value of 16×10^4 is chosen to allow significant flow in the mushy region while suppressing fluid velocities in the solid region and b is a small number, 10^{-4}, used to prevent the floating point overflow. The source terms Au, Av, and Aw on the right-hand side of the momentum equations were used to model the flow through the porous medium within the solid–liquid interface.[6] For the simulation of isothermal melting, the existence of porous media is hypothetical and used to extinguish the velocities from the liquid to solid regions in a gradual fashion. This ensures a faster convergence.[6]

Energy:

$$\frac{\partial}{\partial t}(\rho\hat{h}) + \frac{\partial}{\partial x}(\rho u\hat{h}) + \frac{\partial}{\partial y}(\rho v\hat{h}) + \frac{\partial}{\partial z}(\rho w\hat{h}) = \frac{\partial}{\partial x}\left(k\frac{\partial T}{\partial x}\right) + \frac{\partial}{\partial y}\left(k\frac{\partial T}{\partial y}\right) + \frac{\partial}{\partial z}\left(k\frac{\partial T}{\partial z}\right) + Q \tag{6}$$

The enthalpy $\hat{h}$ can be written as a summation of the sensible component $h_s = C_p T$ and the latent heat component ΔH, so that the total enthalpy is defined as $\hat{h} = h_s + \Delta H$. For an isothermal melting problem, the latent heat component ΔH is given by the following function:

$$\Delta H = \begin{cases} L, & \text{if} \quad T > T_m \\ 0, & \text{if} \quad T < T_m \end{cases} \tag{7}$$

Substituting this expression into Eq. (5) the following final form of the energy equation is formulated:

$$\frac{\partial}{\partial t}(\rho c_p T) + \frac{\partial}{\partial x}(\rho u c_p T) + \frac{\partial}{\partial y}(\rho v c_p T) + \frac{\partial}{\partial z}(\rho w c_p T) = \frac{\partial}{\partial x}\left(k\frac{\partial T}{\partial x}\right) + \frac{\partial}{\partial y}\left(k\frac{\partial T}{\partial y}\right) + \frac{\partial}{\partial z}\left(k\frac{\partial T}{\partial z}\right) - \frac{\partial}{\partial t}(\rho\Delta H) + Q \tag{8}$$

Heat generation at the faying surface was considered as a volumetric heat source with a small effective thickness (0.05 mm) (Ref. 12). A cylindrical shaped solid (of radius r_e) within the workpieces between the two electrodes was considered to act as a source for joule heating. All of the control volumes that take part in heat generation had an additional term Q (volumetric heat source) on the right-hand side of their energy equation (8). Control volumes (except the faying surface control volumes) that take part in joule heating had the additional volumetric heat source term

$$Q = \frac{I^2}{\pi^2 r_e^4 \sigma} \tag{9}$$

where $I = I_m \sin(120\pi t)$ represents the maximum amplitude of the ac current. The faying surface control volumes participated in joule heating in addition to generating heat due to current flow through the electric contact resistance. The contact resistance was assumed to vary as a linear function of temperature.[8,13,18] The additional volumetric source term for the faying surface control volumes is given by

$$Q = \frac{I^2}{\pi^2 r_e^4 \sigma} + \frac{I^2 R_\infty}{\pi r_e^2 \varepsilon_f}\left(\frac{T_m - T}{T_m - T_\infty}\right) \tag{10}$$

where the terms represent joule heating and interfacial heating due to contact resistance, respectively.

Calculation Domain and Boundary Conditions

A $20 \times 20 \times 2.09$ mm solid domain having a 50-μm initial, effective gap between the workpieces was defined for the spot welding model. A schematic diagram of the central vertical plane for the workpiece calculation domain and boundaries is presented in Fig. 2. The outer surfaces of the workpieces that were not in contact with the electrode experienced natural convection with the ambient. Heat losses due to the convection of air at the boundaries are defined as follows with a constant, average convection coefficient h based on the representative ΔT:

$$h(T_{\mathrm{wps}} - T_\infty) = -k_{\mathrm{wp}}\left(\frac{\partial T_{\mathrm{wp}}}{\partial \hat{n}}\right) \tag{11}$$

A major heat loss resulted from the conduction of heat through the electrodes. The electrodes have coolant jackets that extracted the heat generated within the workpieces. Heat transfer from the workpieces to the electrodes is given by the following:

$$U_e(T_{\mathrm{wp}} - T_e) = -k_{\mathrm{wp}}\left(\frac{\partial T_{\mathrm{wp}}}{\partial \hat{n}}\right) \tag{12}$$

The initial workpieces and electrode temperatures were assumed to be the ambient temperature. This is a reasonable approximation of the actual conditions experienced in resistance welding because the heat dissipates rapidly from copper to the coolant water flowing through the electrodes.

Numerical Procedures

The momentum and energy conservation equations were solved numerically, utilizing the iterative SIMPLER algorithm.[19] This algorithm was based on the fully implicit finite volume technique. The latent heat content of each control volume was updated after each iteration, using the temperature field predicted by the energy equation.[6] A thorough grid refinement test was performed by successively refining the mesh. A comparison of the solution for meshes consisting of 121 × 43 × 121 and 99 × 43 × 99 nodes is documented. The temperatures within the molten region differed by a maximum of 1.5%, whereas those of the solid region ranged from 0 to 5% with isolated, anomalous points of 5.8% difference. The maximum temperature difference, occurring at a few isolated nodes along the interface of the solid and liquid regions at the faying surface, is 7.8%. These differences lead to the comparison of molten pool volumes. Whereas the molten pool thicknesses agreed, the diameters varied by a maximum of only 3.8% at the faying surface. As a result, the 99 × 43 × 99 configuration was used to model the workpieces. Control volume nodes were uniformly distributed in the x and z directions but nonuniformly distributed in the y direction due to the presence of the interfacial effective gap ε_f between the workpieces. The electrodes were modeled in two dimensions using a uniform mesh of 23 × 43 nodes. Fully implicit, dynamic time stepping was developed to use efficiently computer resources and to prevent divergence. The initial time step, set at 1×10^{-5} s, was adjusted after every 25 steps based on the average iterations required for convergence and state of the welding current. The time steps were limited while the current increased, up to 3.75 cycles, but allowed to grow while the current decreased, after 3.75 cycles. A restart file was used to restart the program in the event of diverging iterations. In this situation, a ceiling was established at approximately 80% of the diverging time step. When the time step reached this ceiling, it was not allowed to increase further for approximately 500 steps. In this manner, optimum time steps were determined by the program for each run of the parametric study. The relaxation factors used for the momentum and energy equations were 0.2 and 0.9, respectively. The pressure and pressure correction equations were not relaxed at all. Convergence was declared for temperature when the ΔT between successive iterations fell below 1×10^{-4}.

Results and Discussion

A parametric study was performed to determine the influence of various welding parameters including current, faying surface electrical contact resistance, E/W thermal contact conductance, and E/W contact area. Weld pool dynamics during nugget formation, velocity fields in the molten pool, and trends of nugget growth were also investigated. Experiments were performed on 1.04-mm-thick, 1000-series aluminum sheets to validate the proposed RSW model. The weld schedule (Fig. 3) was used with the maximum amplitude of 45-kA alternating current. Cone-shaped electrodes with 18-deg cone angles and 2.0-rad spherical faces (approximately 9.90-mm-diam tip) were used in the experiments. A summary of the different cases studied is listed in Table 1. Cases A, B, and C were used to illustrate the influence of E/W contact conductance; cases A, D, E, and F to show the effects of welding current; and cases A, G, and H to investigate faying surface electrical contact resistance. The numerical results of pure aluminum are comparable to the experimental results in Al 1000 because the purity is approximately 99%.

Test case A (Table 1) was used to compare the experimentally obtained nugget geometry with that predicted by the numerical simulation. This case consisted of a static contact resistance of 450 $\mu\Omega$ at the faying surface, a thermal contact conductance of 20 kW/m^2-K at the E/W interface, a 45-kA maximum alternating current, and a 9.90-mm-diam flat-faced electrode. Tables 2 and 3 list the property values and welding conditions for the workpieces and the electrodes. The experimental and numerical results for case A are compared in Figs. 4 and 5 for the nugget thickness and diameter, respectively. A digital camera, with an aspect ratio of 1:1, was used to photograph the cross-sectional views of the welded joints. The microhardness indent shown in Fig. 5a is 0.652 mm in length. This indention was used to measure the experimental nugget thickness and diameter. The thickness and diameter of the nugget found from the experiment are 0.532 and 2.466 mm, respectively, whereas those for the numerical simulations are 0.426 and 2.246 mm, respectively. The experimental nugget was not perfectly round, and therefore, an average diameter was used for the comparison. The experimental uncertainty in measuring nugget geometry using the Kline–McKlintock method[20] is determined to be about ±3%. This uncertainty does not include the uncertainty associated with the actual welding process. The deviation of the numerical simulation from experimental

Table 1 Test cases for the parametric study of RSW

Test case	FCR, $\mu\Omega$	E/W contact conductance, kW/m^2-K	Maximum current, kA	Resulting weld nugget Thickness, mm	Resulting weld nugget Diameter, mm
A	450	20	45	0.426	2.245
B	450	15	45	0.989	3.905
C	450	10	45	1.593	5.278
D	450	20	47	0.776	3.787
E	450	20	49	1.035	4.416
F	450	20	51	1.326	4.951
G	350	20	45	0.162	1.165
H	550	20	45	0.437	2.553

Table 2 Welding conditions for aluminum RSW

Property	Value
Workpiece material	Al 1000
Electrode material	Copper
Ambient and coolant temperature, °C	30.0
Separation gap between workpieces, m	5×10^{-5}
Heat transfer coefficient at workpiece boundaries, W · m^{-2}-K^{-1}	15.0
Heat transfer coefficient at electrode-coolant hole, W · m^{-2}-K^{-1}	1.0×10^6
Gap between electrode surface and coolant, m	3×10^5

Table 3 Properties of aluminum and copper

Property	Aluminum	Copper
Density, kg · m^{-3}	2,365.75	9,000
Volumetric thermal coefficient of liquid	69.3×10^{-6}	——
Thermal conductivity, W · m^{-1} K^{-1}	211.43	400
Melting point, °C	660.3	1,357
Latent heat of fusion, J · kg^{-1}	397,000	——
Specific heat capacity, J · kg^{-1}	1,339.78	390
Dynamic viscosity, kg · m^{-1} s^{-1}	1.286×10^{-6}	——
Electrical conductivity, mho · m^{-1}	——	5.9×10^7

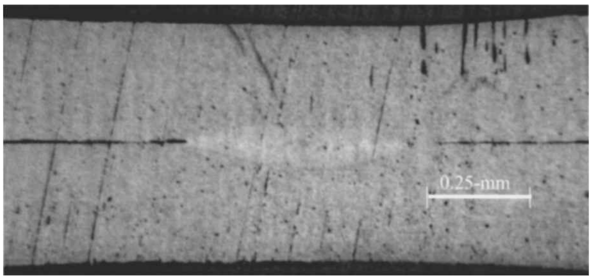

a) Experimental

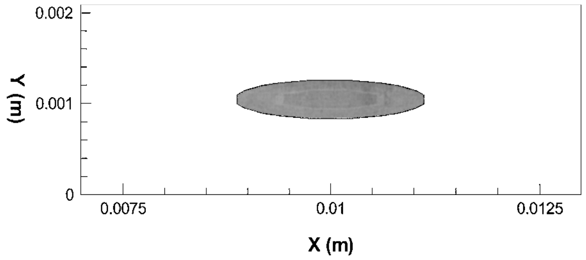

b) Numerical

Fig. 4 Comparison of experimental and numerical nugget thickness in the central vertical plane for RSW of 1.04-mm-thick aluminum sheets: test case A.

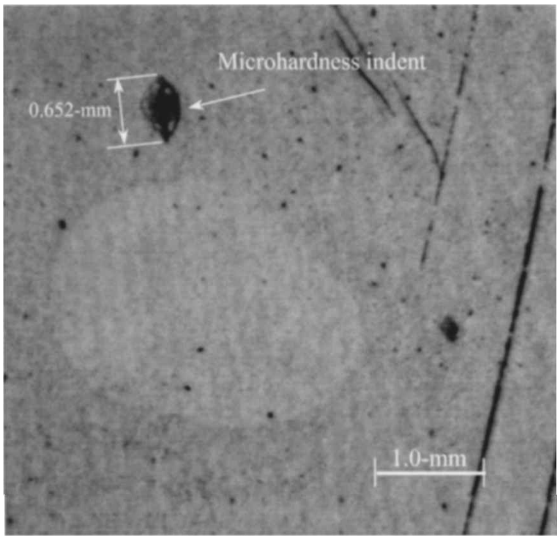

a) Experimental

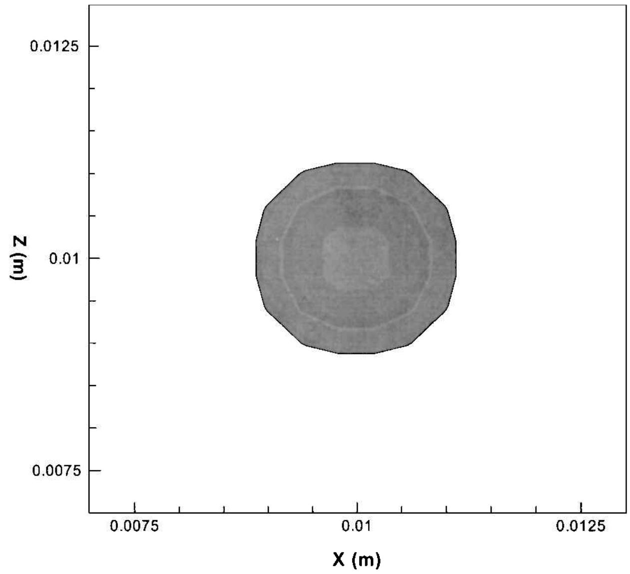

b) Numerical

Fig. 5 Comparison of experimental and numerical nugget diameter in the central horizontal plane (along the faying surface) for 1.04-mm-thick aluminum sheets: test case A.

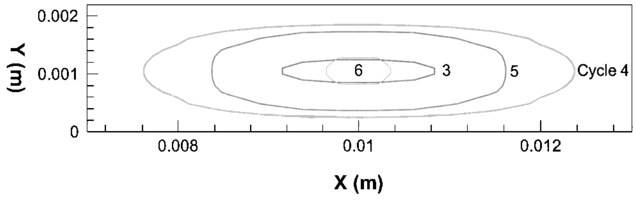

Fig. 6 Variation of weld pool shape with time in the central vertical plane for test case C.

findings is less than 18.0% for nugget thickness and 9.00% for the weld diameter. This deviation arises mainly from errors in the approximation of the electrode geometry. The truncated cone electrodes used in the experiments had spherical radius faces that resulted in smaller contact between the electrodes and workpieces and, consequently, higher current densities than modeled. Despite this slight difference in electrode shape, the results show an acceptable agreement.

Thermal contact resistance occurs at the E/W contact surface due to surface roughness and oxide layers. The value of this thermal contact resistance depends on the applied electrode pressure, the type of metals in contact, and the area of contact.[21–24] The electrodes enhance solidification of the weld pool by extracting most of the heat generated within the workpiece. This heat transfer depends on the thermal contact conductance at the E/W interface and, thus, has a significant effect on the melting and solidification processes involved in RSW.

The E/W contact conductance of case A was varied to 15 and 10 kW/m^2-K in cases B and C. Figures 6 and 7 show the variation of weld pool geometry in the vertical and horizontal planes passing through the nugget center, respectively for case C. The weld pools have elliptical shapes in the vertical cross section and are circular in the horizontal cross section. Figures 6 and 7 show the weld pool shapes at the third, fourth, fifth, and sixth cycles, respectively. The fourth cycle illustrates the largest weld pool (before the onset of solidification) and, consequently, the actual nugget formed for case C. The weld pool grows through the melting process until cycle 4, when it begins to solidify. Both melting and solidification occur nonlinearly with time. Figures 8 and 9 show the effect of the relative magnitude of E/W contact conductance on thickness and diameter, respectively, for cases A, B, and C. Because field variables were recorded at quarter cycles, note that melting began between cycles 3.75 and 4.0, 3.25 and 3.5, and 2.75 and 3.0 for cases A, B, and C, respectively. Solidification concluded between cycles 4.5 and 4.75, 5.0 and 5.25, and 6.0 and 6.25 cycles for cases A, B, and C, respectively. As the E/W contact conductance increased in value, the initiation of melting was delayed, and solidification occurred more rapidly. This is physically reasonable because a higher contact conductance allows more heat to be extracted by the coolant fluid in the electrodes. The maximum weld pool thickness is found to be 0.99 and 1.6 mm at cycle 4 for cases B and C, respectively. However, the maximum weld pool thickness found for case A is 0.43 mm at 4.25 cycles. The maximum weld pool diameters are 2.25, 3.91, and 5.28 mm for cases A, B, and C, respectively. The lower values of E/W contact conductance result in larger nugget volumes.

Figure 10 shows the three-dimensional workpiece temperature field for test case B (15-kW/m^2-K) at cycle 4, sectioned for clarity. The temperature field is axisymmetric, and the maximum temperature is found at the faying surface. Conduction through the electrodes reduces the temperature near the E/W contact surface. As the value of E/W contact conductance increases, the volume of the molten pool decreases. High E/W contact conductance permits greater heat transfer through the electrodes and the heat-affected zone (HAZ) reduces gradually with increases in E/W contact conductance.

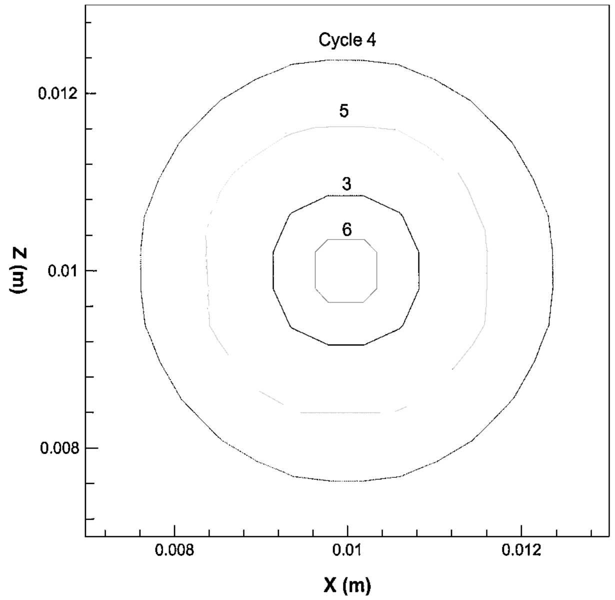

Fig. 7 **Variation of weld pool shape with time in the horizontal plane along the faying surface for test case C.**

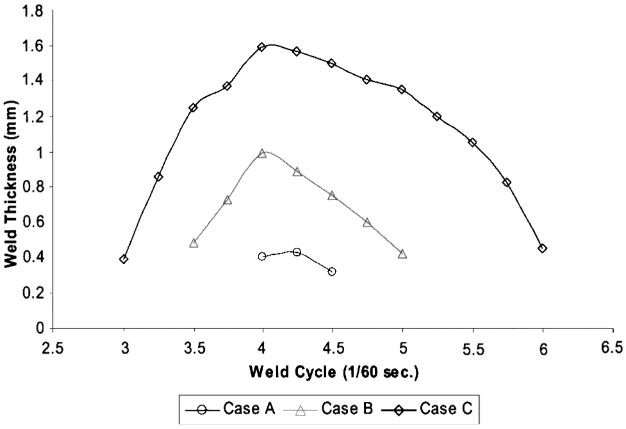

Fig. 8 **Effects of E/W contact conductance on transient nugget thickness.**

Four different currents (with maximum amplitudes of 45, 47, 49, and 51 kA) were used to study the effect of current on RSW with test cases A, D, E, and F. The base variables of case A, as described in Table 1, were used for the comparisons of current. Figures 11 and 12 show the effects of current on weld nugget thickness and diameter. Heat generation in the workpieces and electrodes rises with increases in current because the heat produced by joule heating is proportional to the square of the welding current. Melting initiation time varies as a function of current as well. Melting begins between cycles 2.75 and 3 for the 51-kA current, case F. For 49 kA, case E, the melting begins between cycles 3 and 3.25, whereas it is bounded by cycles 3.5 and 3.75 for 47 kA, case D. Solidification begins after the weld pool thickness reaches a maximum value at cycle 4. Weld pool solidification for the 47-, 49-, and 51-kA currents ends between cycles 4.75 and 5.0, 5.0 and 5.25, and 5.25 and 5.5, respectively. The maximum weld pool thickness are 1.33, 1.04, and 0.78 mm for the 51-, 49-, and 47-kA currents, respectively. The time for which the weld pool remains molten increases with the increase of current. As the current increases, the volume of the weld pool, as well as the HAZ at cycle 4, increases, although the increment is nonlinear.

Figure 13 shows the vertical plane velocity field development for case F (51-kA current) during RSW of aluminum. It is observed that the vertical field velocities are almost one order of magnitude larger than those of the horizontal field velocities. Prominent convection cells that govern the molten pool dynamics during RSW appear in

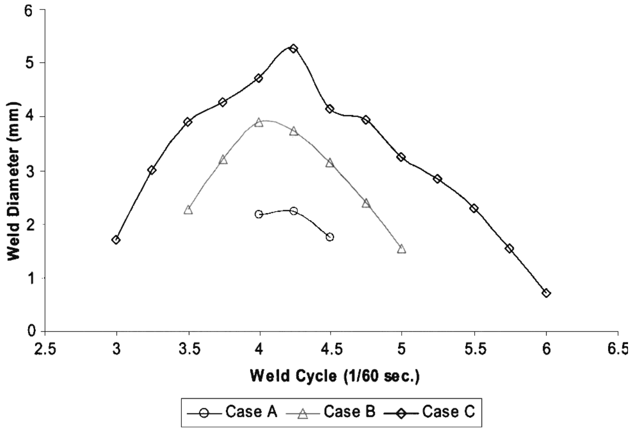

Fig. 9 **Effects of E/W contact conductance on transient nugget diameter.**

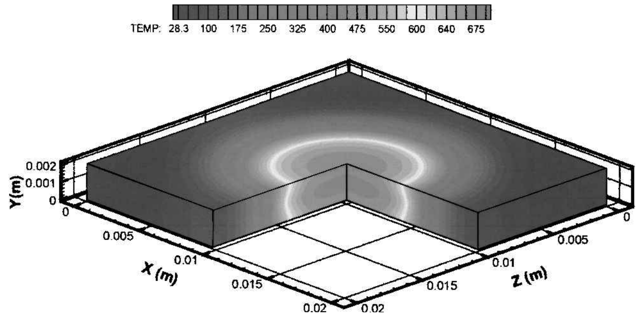

Fig. 10 **Workpiece temperature field sectioned to present internal temperatures at cycle 4 for test case B.**

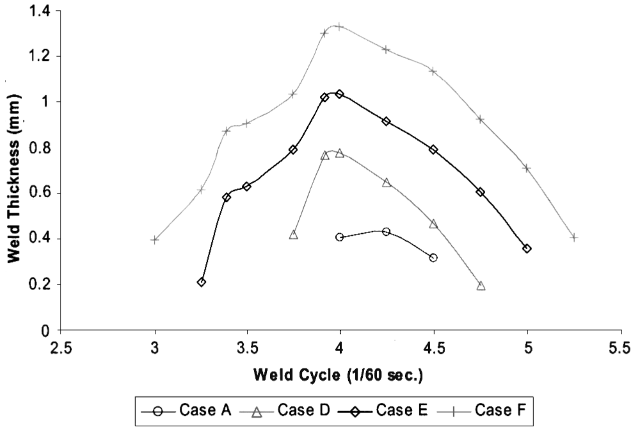

Fig. 11 **Effects of current on transient nugget thickness.**

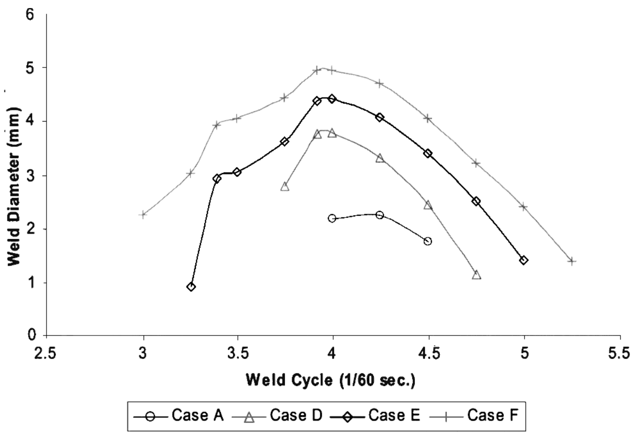

Fig. 12 **Effect of current on transient nugget diameter.**

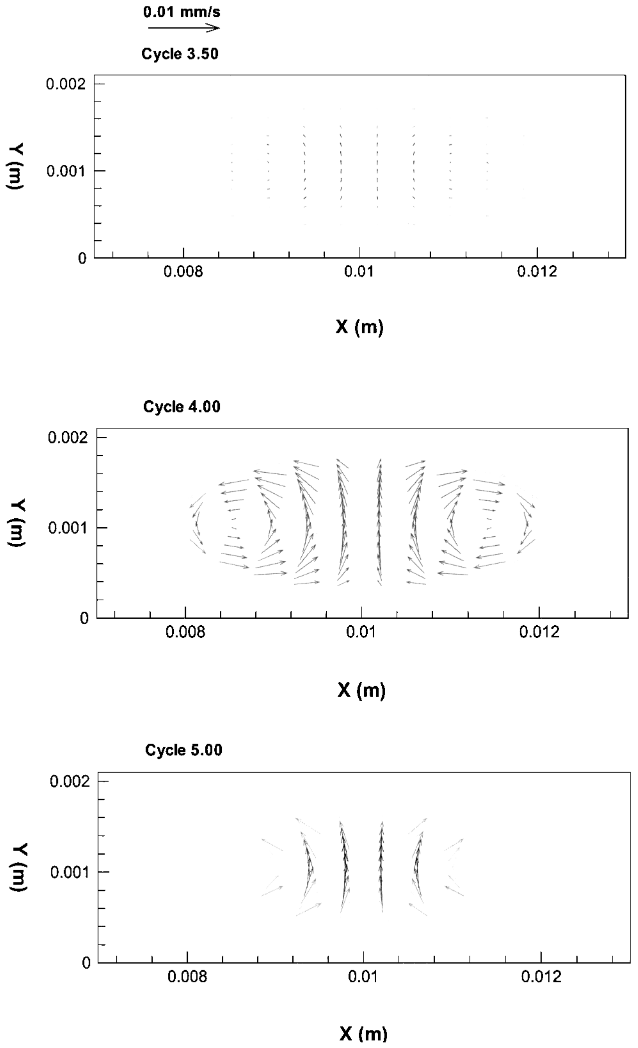

Fig. 13 Velocity field development with time in the central vertical plane for test case F.

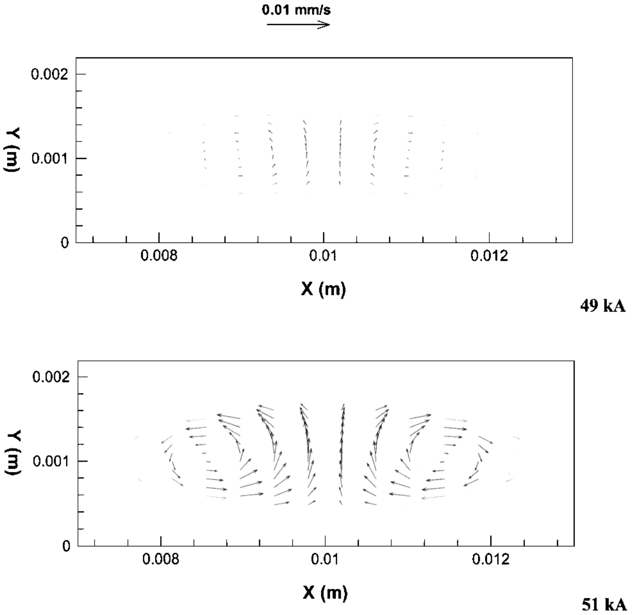

Fig. 14 Effect of current on velocity fields in the central vertical plane (cycle 4) for test cases E and F.

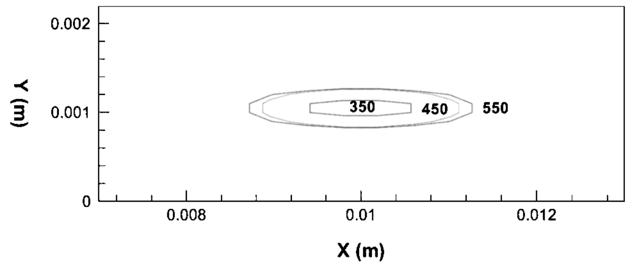

Fig. 15 Effects of faying surface contact resistance on nugget shape in the central vertical plane for test cases A, G, and H.

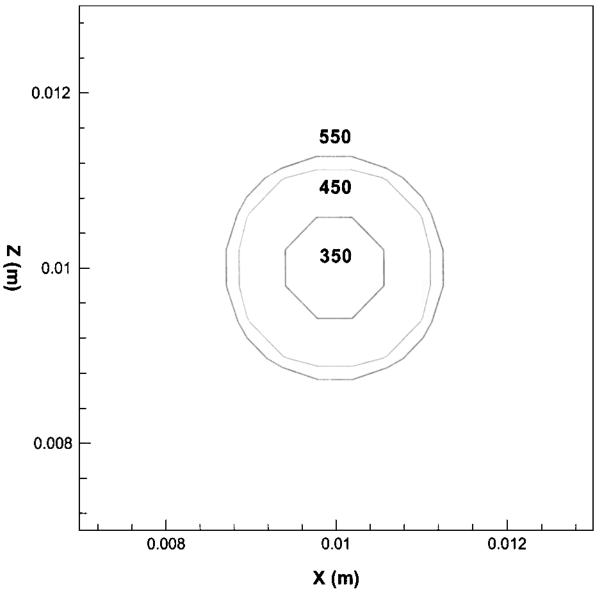

Fig. 16 Effects of faying surface contact resistance on nugget shape in the horizontal plane along the faying surface for test cases A, G, and H.

the vertical plane. At cycle 3.5, the velocity field has just begun to grow; the velocities are small, and distinguishable convection cells are not found. The molten pool continues to grow until cycle 4, when two prominent convection cells are established in the vertical plane. Molten metal moves upward along the centerline axis of the molten pool before flowing radially outward and finally downward along the walls of the weld pool, driven by buoyancy forces. The maximum velocities encountered at cycle 4 are close to 0.008 mm/s. The convection cells begin to disappear as solidification starts. The velocities are very small and, thus, have little effect on the nugget geometry.

Figure 14 shows the effect of variation of welding current on the vertical plane velocity fields at cycle 4. The molten pool does not have sufficient time to generate a velocity field or convection cell for the 47-kA current, case D (not shown). For 49 kA, case E, the convection cells are barely visible. The velocities and convection cells become dominant with an increase in current. A 51-kA current, case F, shows two convection cells and maximum velocity of 0.008 mm/s. Similar effects are found for the variation of current in the horizontal plane velocity fields. The molten pool size increases with current, leading to the larger velocity field. The velocities found in the horizontal planes are an order of magnitude smaller than those encountered in the vertical plane.

Faying surface–electrical contact resistance (FCR) is important for nugget initiation. For the current RSW model, FCR is a function of the static contact resistance [Eq. (10)]. This static contact resistance was varied in cases G and H to study the effect of FCR in RSW. Figure 15 shows the effect of FCR on nugget geometry in the vertical plane. For a 350-$\mu\Omega$ FCR (case G), a tiny nugget of 0.16 mm thickness is formed. It is interesting to observe that the nugget thickness for the 450- and 550-$\mu\Omega$ FCR, cases A and H, is around 0.43 mm, although they exhibit different shapes. Higher

FCR values lead to larger nugget sizes. Figure 16 shows the effect of FCR on nugget shape and diameter in the horizontal plane, along the faying surface. Nugget diameters for 550-, 450-, and 350-$\mu\Omega$ faying surface contact resistances (cases G, A, and H) are 1.16, 2.25, and 2.55 mm, respectively. As expected with the variation of FCR, interface heat generation also varies, leading to differing nugget sizes. The temperature fields resulting from the variation of FCR are nearly indistinguishable, illustrating that this parameter has a lesser effect on RSW than the others considered.

Conclusions

RSW in pure aluminum with realistic three-dimensional boundary conditions and molten pool convection was successfully modeled. The predicted numerical results were successfully compared with experimental findings. Electrode wear, occurring in industrial applications of RSW, leads to asymmetric contact with the workpieces that can be captured by the developed model.

The length of time that the weld pool exists is directly proportional to current and indirectly proportional to E/W thermal contact conductance. Nugget size increases nonlinearly with the increase in current and faying surface electrical contact resistance, but decreases with the increase of E/W thermal contact conductance. The influence of the FCR on nugget size is less pronounced than the other parameters studied. The maximum weld pool is found to be of the order of 0.01 mm/s in this study. The vertical plane velocity is found to be an order of magnitude higher than that of the horizontal plane within the molten pool. The size of the three-dimensional elliptical HAZ at the workpiece center is inversely proportional to the E/W thermal contact conductance, whereas it is directly proportional to the welding current and faying surface contact resistance.

The proposed model can be used to develop optimum welding schedules for varying conditions. The transient temperature history obtained from the present study could be effectively used to predict microstructure within the nugget and the HAZ.

Acknowledgments

Acknowledgments are due to the National Science Foundation and the South Carolina Experimental Program to Stimulate Competetive Research for financial support and to NASA Langley Research Center, Hampton, Virginia, for the experimental facilities and assistance provided for this research.

References

[1] Viskanta, R., "Natural Convection in Melting and Solidification," *Natural Convection: Fundamentals and Applications*, Hemisphere, Washington, DC, 1985, pp. 845–877.

[2] Viskanta, R., "Heat Transfer During Melting and Solidification of Metals," *Journal of Heat Transfer*, Vol. 110, No. 4, 1988, pp. 1205–1219.

[3] Viskanta, R., "Phase Change Heat Transfer in Porous Media," *Proceedings of the Third International Symposium on Cold Region Heat Transfer*, edited by J. P. Zarling and S. L. Faussett, Univ. of Alaska, Fairbanks, AK, 1991, pp. 1–24.

[4] Yao, L. S., and Prusa, J., "Melting and Freezing," *Advances in Heat Transfer*, Vol. 19, 1989, pp. 1–95.

[5] Fukusako, S., and Yamada, M., "Recent Advances in Research on Melting Heat Transfer Problems," *Heat Transfer*, 1991, pp. 313–330.

[6] Brent, A. D., Voller, V. R., and Reid, K. J., "Enthalpy Porosity Technique for Modeling Convection–Diffusion Phase Change: Application to the Melting of Pure Metal," *Numerical Heat Transfer*, Vol. 13, No. 3, 1988, pp. 297–318.

[7] Gau, C., and Viskanta, R., "Melting and Solidification of a Pure Metal on a Vertical Wall," *Journal of Heat Transfer*, Vol. 108, No. 1, 1986, pp. 174–181.

[8] Gould, J. E., "An Examination of Nugget Development During Spot Welding, Using Both Experimental and Analytical Techniques," *Welding Journal*, Vol. 66, No. 1, 1987, pp. 1-s–10-s.

[9] Nied, H. A., "The Finite Element Modeling of the Resistance Spot Welding Process," *Welding Journal*, Vol. 63, No. 4, 1984, pp. 123-s–132-s.

[10] Tsai, C. L., Jammal, O. A., Papritan, J. C., and Dickinson, D. W., "Modeling of Resistance Spot Weld Nugget Growth," *Welding Journal*, Vol. 71, 1992, pp. 47-s–54-s.

[11] Browne, D. J., Chandler, H. W., Evans, J. T., and Wen, J., "Computer Simulation of Resistance Spot Welding in Aluminum: Part I," *Welding Journal*, Vol. 74, No. 10, 1995, pp. 339-s–344-s.

[12] Wei, P. S., and Ho, C. Y., "Axisymmetric Nugget Growth During Resistance Spot Welding," *Journal of Heat Transfer*, Vol. 112, No. 2, 1990, pp. 309–316.

[13] Wei, P. S., and Yeh, F. B., "Factors Affecting Nugget Growth with Mushy Zone Phase Change During Resistance Spot Welding," *Journal of Heat Transfer*, Vol. 113, No. 3, 1991, pp. 643–649.

[14] Wei, P. S., Wang, S. C., and Lin, M. S., "Transport Phenomena During Resistance Spot Welding," *Journal of Heat Transfer*, Vol. 118, No. 3, 1996, pp. 762–773.

[15] Tsai, C. L., "Advances in the Resistance Welding of Automotive Aluminum," *Journal of the Minerals, Metals and Materials Society*, Vol. 49, No. 5, 1997, pp. 28–30.

[16] Xu, L., and Khan, J. A., "The Finite Element Modeling of Axisymmetric Nugget Development During Resistance Spot Welding," *Proceedings of the 5th International Conference on Trends in Welding Research*, edited by J. M. Vitek, S. A. David, J. A. Johnson, H. B. Smartt, and T. S. DebRoy, ASM International, Materials Park, OH, 1998, pp. 616–621.

[17] James, P. S., "Electrical Contact Resistance: Observations Relevant to the Spot Welding of Aluminum Alloys," Ph.D. Dissertation, Mechanical Engineering, Univ. of Newcastle upon Tyne, Newcastle upon Tyne, England, U.K., 1995.

[18] Vogler, M., and Sheppard, S., "Electrical Contact Resistance Under High Loads and Elevated Temperatures," *Welding Journal*, Vol. 72, No. 6, 1993, pp. 231-s–239-s.

[19] Patankar, S. V., *Numerical Heat Transfer and Fluid Flow*, Hemisphere, Washington, DC, 1980.

[20] Kline, S. J., and McClintock, F. A., "Describing Uncertainties in Single Sample Experiments," *Mechanical Engineering*, Vol. 75, No. 1, 1953, pp. 385–387.

[21] Peterson, G. P., and Fletcher, L. S., "Measurement of the Thermal Contact Conductance and Thermal Conductivity of Anodized Aluminum Coatings," *Journal of Heat Transfer*, Vol. 112, No. 3, 1990, pp. 579–585.

[22] Lambert, M. A., Marotta, E. E., and Fletcher, L. S., "The Thermal Contact Conductance of Hard and Soft Coat Anodized Aluminum," *Journal of Heat Transfer*, Vol. 117, No. 2, 1995, pp. 270–275.

[23] Fletcher, L. S., "Recent Developments in Contact Conductance Heat Transfer," *Journal of Heat Transfer*, Vol. 110, No. 4, 1988, pp. 1059–1070.

[24] Madhusudana, C. V., and Fletcher, L. S., "Contact Heat Transfer—The Last Decade," *AIAA Journal*, Vol. 24, No. 3, 1985, pp. 510–523.